Magnetic Resonance Imaging 60 (2019) 101–109

Contents lists available at ScienceDirect

Magnetic Resonance Imaging

journal homepage: www.elsevier.com/locate/mri

Original contribution

Compressed sensing MRI based on image decomposition model and group sparsity

Xiaoyu Fan[a,b,c], Qiusheng Lian[a,c,*], Baoshun Shi[a,c]

[a] School of Information Science and Engineering, Yanshan University, Qinhuangdao 066004, China
[b] School of Electrical and Electronic Engineering, Anhui Science and Technology University, Chuzhou 233100, China
[c] Hebei Key Laboratory of Information Transmission and Signal Processing, Yanshan University, Qinhuangdao 066004, China

ARTICLE INFO

Keywords:
MR image reconstruction
Image cartoon-texture decomposition
Adaptive tight frame
Group sparsity
Total variation

ABSTRACT

The image representation plays an important role in compressed sensing magnetic resonance imaging (CSMRI). However, how to adaptive sparsely represent images is a challenge for accurately reconstructing magnetic resonance (MR) images from highly undersampled data with noise. In order to further improve the reconstruction quality of the MR image, this paper first proposes tight frame-based group sparsity (TFGS) regularization that can capture the structure information of images appropriately, then TFGS regularization is employed to the image cartoon-texture decomposition model to construct CSMRI algorithm, termed cartoon-texture decomposition CSMRI algorithm (CD-MRI). CD-MRI effectively integrates the total variation and TFGS regularization into the image cartoon-texture decomposition framework, and utilizes the sparse priors of image cartoon and texture components to reconstruct MR images. Virtually, CD-MRI exploits the global sparse representations of image cartoon components by the total variation regularization, and explores group sparse representations of image texture components via the adaptive tight frame learning technique and group sparsity regularization. The alternating iterative method combining with the majorization-minimization algorithm is applied to solve the formulated optimization problem. Finally, simulation experiments demonstrate that the proposed algorithm can achieve high-quality MR image reconstruction from undersampled K-space data, and can remove noise in different sampling schemes. Compared to the previous CSMRI algorithms, the proposed approach can lead to better image reconstruction performance and better robustness to noise.

1. Introduction

Magnetic resonance imaging (MRI) has been employed in the basic science research and clinical practical diagnosis because of its non-invasive and nonionizing imaging property [1–3]. Therefore, the legible MR images should be provided for the basic imaging experiment and clinical medical inspection associated with disease state. To reconstruct high-quality MR images, the data sampling rate of the traditional MRI method needs to satisfy Shannon-Nyquist sampling theorem which suffers from large amounts of sampling data and long data acquisition time. Hence, how to minimize the amount of acquisition data and shorten the sampling time for achieving accurate reconstruction of the MR image, is a key issue. Since MR images are sparse in certain transform domain, the compressed sensing (CS) theory presented by Donoho [4] and Candes et al. [5] in 2006, can be utilized to recover MR images from highly undersampled K-space data [6–9]. Meanwhile, the CS theory used for MRI can speed up the image sampling. However, how to exploit more sparsity-induced regularization is a challenge for researchers to construct CSMRI algorithms. Recently, researchers have developed lots of advanced algorithms to accurately reconstruct MR images.

Lusting et al. [10] first utilized CS to reconstruct MR images in spatial domain, and proposed a CSMRI algorithm based on the total variation (TV) regularization which describes the gradient sparsity of images. Kim et al. [11] presented a CSMRI algorithm in which the dual-tree complex wavelet transform acts as the global sparse prior regularization to recover images with directional structures. Qu et al. [12] exploited the contourlet transform as sparsity regularization to achieve better reconstruction quality of MR image with curve and contour features. However, the above CSMRI algorithms just adapt for accurately reconstructing MR images with special features, since sparse priors selected by the algorithms have certain limitations by their own. In order to further promote image reconstruction performance, researchers have taken into account fusing various sparse priors together

* Corresponding author at: School of Information Science and Engineering, Yanshan University, Qinhuangdao 066004, China.
E-mail address: lianqs@ysu.edu.cn (Q. Lian).

https://doi.org/10.1016/j.mri.2019.03.011
Received 16 December 2018; Received in revised form 18 February 2019; Accepted 10 March 2019

into CSMRI algorithms. For example, Qu et al. [13] employed sparse representations of the wavelet transform and contourlet transform regularization to improve the reconstruction quality of MR images. Huang et al. [14] applied the wavelet transform and TV regularization for speeding up MR image reconstruction. Chen et al. [15] combined the wavelet sparsity, gradient sparsity and tree sparsity together to form a fast optimal CSMRI algorithm; Huang et al. [16] merged the wavelet transform regularization, TV regularization and nonlocal self-similarity constraint into a CSMRI algorithm; and the two algorithms can enhance the precision of MR image reconstruction.

The sparse representations of all the approaches mentioned above are non-adaptive for MR images, which has some limitations upon recovering images from highly undersampled K-space data. For promoting the self-adapted ability of CSMRI algorithms, adaptive sparse representation methods were exploited for reconstructing the MR image. Ravishankar et al. [1] presented the adaptive dictionary learning CSMRI algorithm (DLMRI) based on the K-SVD method. The transform learning CSMRI algorithm (TLMRI) was introduced to simultaneously reconstruct the image and learn adaptive sparsifying transform in [17]. Liu et al. [18] proposed a CSMRI algorithm for recovering MR images by using the adaptive synthesis dictionary learned in gradient domain. In [19], an inversion algorithm exploiting the adaptive Bayesian dictionary learning of the beta-Bernoulli process was proposed for CSMRI. Moreover, some CSMRI algorithms based the adaptive tight frame (ATF) also had been introduced to recover MR images, for example the data-driven tight frame CSMRI approach (DDTF-MRI) [20] and the two-layer tight frame sparsifying model (TRIMS) [21]. Liu et al. presented the projected fast iterative soft-thresholding algorithm (pFISTA) to rapidly reconstruct the MR image in [22]. In order to prevent losing important spatial structures and ignoring the consistency of pixels for MR images, the convolutional operation of sparse coding method as sparsity regularization was utilized to CSMRI algorithms such as the convolutional sparse coding in gradient domain (GradCSC) [23] and the convolutional sparse coding in fields-of-experts (FoECSC) [24]. The adaptive CSMRI algorithms can achieve the superior performance for reconstructing MR images.

The sparsity of the MR image measured by the aforementioned approaches is the normal global sparsity. In addition to the proposal normal global sparsity mentioned above, the group sparsity which is the extension of the normal global sparsity for CS [25] can explore some sparse priors including the sparsity of the image, local similarity of the image and so on. Hence, as a certain kind of sparse priors, the group sparsity has been widely used in the image processing realm, such as image denoising and MR image reconstruction. To increase the degree of sparsity of MR images, some researchers have proposed lots of group sparsity regularization-based CSMRI algorithms, for instance, Jin et al. [26], Jiang et al. [27], Liu et al. [28], Liu et al. [29] and Yu et al. [30]. The algorithms built on the group sparsity can acquire better MR image reconstruction quality as well.

The algorithms mentioned above take aim at the undecomposed MR image, and do not take into account the image decomposition theory. However, the image decomposition theory, especially image cartoon-texture decomposition model, has been actually employed in image processing field including image denoising, image decomposition, MR image reconstruction, etc. In [31], Meyer presented the image cartoon-texture decomposition model, but this model cannot be tackled directly. Subsequently, according to Meyer cartoon-texture model, some researchers proposed many image processing algorithms based on CS for sparsely representing diverse image components. Elad et al. [32] applied sparse representations for the image morphological component analysis decomposition method. In [33], two different components of images were represented sparsely in term of two different synthesis dictionaries, respectively. Tu et al. [34] developed the image cartoon-texture decomposition model to automatic trace and segment fat pads of MR images, and the model accomplished precise delineation of mammary pads. In 2010, Peyre et al. [35] designed the image cartoon-texture decomposition model in which image cartoon components were represented sparsely by using fixed global dictionary and image texture components were represented sparsely by learning adapted local dictionary. In order to better segregate different components from images, Li et al. in literature [36] described an improved learning algorithm for recovering images, and the algorithm can simultaneously handle dictionary learning of two components and image reconstructions. Zhang et al. [37] exploited the convolutional sparse coding and convolutional low-rank coding approaches to decompose cartoon and texture components from given images, the algorithm directly applied shift-invariance property to the cost function for training filters, and simulation experiments of the algorithm achieved superior performance.

The contribution of this paper is that we first propose a TFGS regularization that coalesces ATF learning technique and group sparsity together. Then, TFGS regularization is used to the image cartoon-texture decomposition framework for accurately reconstructing MR images. To further improve image reconstruction performance, this paper presents a novel CSMRI algorithm dubbed CD-MRI which integrates TV and TFGS regularization into the same image cartoon-texture decomposition model. CD-MRI can acquire the cartoon part of the MR image via TV regularization, and simultaneously reconstruct the texture part by employing ATF and group sparsity methods. The simulation experiment results demonstrate that the proposed algorithm can accurately reconstruct MR images from highly undersampled noisy measurement data.

The remainder of the paper is organized as follows: Section 2 describes the preliminary knowledge about the image cartoon-texture decomposition theory, group sparsity and ATF learning technique; Section 3 proposes our CD-MRI algorithm of the MR image reconstruction; Section 4 verifies that the proposed algorithm has the good ability for enhancing reconstruction quality of MR images by various simulation experiments; and Section 5 gives the conclusions and future works.

2. Background

In this section, we briefly review some CS theoretical frameworks including the image cartoon-texture decomposition model, group sparsity and ATF learning method for image processing. The following symbol conventions are employed throughout this full paper. $\boldsymbol{x} \in \boldsymbol{R}^{\mathrm{N}}$ denotes an underlying image to be reconstructed, $\boldsymbol{F}_u \in \boldsymbol{R}^{\mathrm{M}\times\mathrm{N}}$ represents the undersampled Fourier coding matrix, $\boldsymbol{y} \in \boldsymbol{R}^{\mathrm{M}}$ denotes the undersampled K-space data of MR images, and λ, λ_1, λ_2 are three positive penalty parameters.

2.1. Image cartoon-texture decomposition model

Image decomposition theory states that images can be decomposed into cartoon and texture components [31,32], which can optimally represent the different components of images. In literature [31], Meyer pointed out that the image cartoon-texture decomposition can be expressed as

$$\boldsymbol{x} = \boldsymbol{u} + \boldsymbol{v}, \tag{1}$$

where $\boldsymbol{u}$ and $\boldsymbol{v}$ represent cartoon and texture components of $\boldsymbol{x}$, respectively. In Eq. (1), $\boldsymbol{u}$ can be modeled by TV, and $\boldsymbol{v}$ can be solved by using the harmonic analysis method. Thereupon, Meyer [31] established the image decomposition model shown as follows

$$\inf_{\boldsymbol{u},\boldsymbol{v}} \{\|\boldsymbol{u}\|_{\mathrm{TV}} + \lambda \|\boldsymbol{v}\|_*, \boldsymbol{u} + \boldsymbol{v} = \boldsymbol{x}\}, \tag{2}$$

where $\|\boldsymbol{u}\|_{\mathrm{TV}}$ denotes the total variation of $\boldsymbol{u}$; $\|\cdot\|_*$ represents the lower bound of l-infinity norm where the infimum is calculated over $\boldsymbol{v}$. However, problem (2) is really difficult to be solved directly. In [38], cartoon and texture components of a given image were decomposed by tackling the following optimal problem

$$\min_{\alpha_1,\alpha_2} \frac{1}{2} \|\boldsymbol{x} - \boldsymbol{D}_1\boldsymbol{\alpha}_1 - \boldsymbol{D}_2\boldsymbol{\alpha}_2\|_2^2 + \lambda_1 \|\boldsymbol{\alpha}_1\|_1 + \lambda_2 \|\boldsymbol{\alpha}_2\|_1 + \lambda \mathrm{TV}(\boldsymbol{D}_1\boldsymbol{\alpha}_1), \tag{3}$$

where $\boldsymbol{D}_1$ and $\boldsymbol{D}_2$ respectively denote the cartoon dictionary and texture dictionary, simultaneously the cartoon and texture components can be represented sparsely via $\boldsymbol{D}_1$ and $\boldsymbol{D}_2$; $\boldsymbol{\alpha}_1$ and $\boldsymbol{\alpha}_2$ are sparse coefficients which respectively coincide with $\boldsymbol{D}_1$ and $\boldsymbol{D}_2$ for the cartoon and texture parts. There are a variety of approaches which have been employed to solve problem (3). Then, one can obtain the cartoon component by calculating $\boldsymbol{u} = \boldsymbol{D}_1\boldsymbol{\alpha}_1$, and acquire the texture component by computing $\boldsymbol{v} = \boldsymbol{D}_2\boldsymbol{\alpha}_2$.

2.2. Group sparsity

In CSMRI algorithm, how to measure the sparsity of the MR image is a crucial issue. As an extension of the normal sparsity, the group sparsity can exploit more effective sparse priors of images [25]. For an MR image, non-zero elements are generally not isolated, but are related to each other and take on as a certain structure [39,40]. Therefore, the adjacent elements can coalesce together as a structure group according to the correlation feature of non-zero elements in the MR image. In general, the structure group with size of $K \times K$ in the normalized MR image $\boldsymbol{x} \in \boldsymbol{R}^{\mathrm{N}}$ can be defined as [41]

$$\widehat{\boldsymbol{x}}_{i,j,K} = \begin{bmatrix} \boldsymbol{x}_{i-m_1,j-m_1} & \boldsymbol{x}_{i-m_1,j-m_1+1} & \cdots & \boldsymbol{x}_{i-m_1,j+m_2} \\ \boldsymbol{x}_{i-m_1+1,j-m_1} & \boldsymbol{x}_{i-m_1+1,j-m_1+1} & \cdots & \boldsymbol{x}_{i-m_1+1,j+m_2} \\ \vdots & \vdots & \ddots & \vdots \\ \boldsymbol{x}_{i+m_2,j-m_1} & \boldsymbol{x}_{i+m_2,j-m_1+1} & \cdots & \boldsymbol{x}_{i+m_2,j+m_2} \end{bmatrix}. \tag{4}$$

Here $\widehat{\boldsymbol{x}}_{i,j,K} \in \boldsymbol{R}^{\mathrm{K}\times\mathrm{K}}$; $m_1 = \lfloor (K-1)/2 \rfloor$, and $m_2 = \lfloor K/2 \rfloor$; $\lfloor \cdot \rfloor$ stands for finding the maximum integer operation. Assume $\boldsymbol{x}_{i,j,K} = \widehat{\boldsymbol{x}}_{i,j,K}(:)$, and the equation designates that all the K column elements of $\widehat{\boldsymbol{x}}_{i,j,K}$ constitute a column vector $\boldsymbol{x}_{i,j,K}$. If employing l_2 norm, the group sparsity of the image can be scaled as following [41]

$$\Phi(\boldsymbol{x}) = \sum_{i,j=1}^{\sqrt{N}} \|\boldsymbol{x}_{i,j,K}\|_2, \tag{5}$$

where the size of the structure group is $K \times K$. Similarly, if exploiting l_1 norm, the group sparsity of the image can be represented in the matrix form as follows

$$\Phi(\boldsymbol{x}) = \|\sqrt{\boldsymbol{H}_{\mathrm{t}}\boldsymbol{x}^2}\|_1, \tag{6}$$

where $\boldsymbol{H}_{\mathrm{t}}$ is the Toeplitz matrix [42] of the box filter.

For an MR image, if utilizing the group sparsity regularization, the underlying image $\boldsymbol{x}$ can be reconstructed from undersampled data $\boldsymbol{y}$ by the following problem formulation

$$\min_{\boldsymbol{x}} \frac{1}{2} \|\boldsymbol{F}_u\boldsymbol{x} - \boldsymbol{y}\|_2^2 + \lambda\Phi(\Psi\boldsymbol{x}). \tag{7}$$

Here Ψ is a certain dictionary or sparsity transform. The term $\|\boldsymbol{F}_u\boldsymbol{x} - \boldsymbol{y}\|_2{}^2$ denotes the data fidelity in K-space, and is used to well adjust the reconstruction error of the MR image. Problem (7) has the good ability for group sparse representations of MR images, and it can achieve better reconstruction performance for the MR image.

2.3. Adaptive tight frame

The tight frame can be used to sparsely represent images. Cai et al. in literature [43] brought up an approach to construct an adaptive tight frame termed data-driven tight frame (DDTF), and DDTF can be directly acquired from the input image via the following optimization problem

$$\min_{\boldsymbol{W},\boldsymbol{v}} \|\boldsymbol{v} - \boldsymbol{W}\boldsymbol{x}\|_2^2 + \lambda \|\boldsymbol{v}\|_0 s.\ t.\ \boldsymbol{W}^{\mathrm{T}}\boldsymbol{W} = \mathbf{I}, \tag{8}$$

where $\boldsymbol{W}$ represents a desired DDTF which can be constituted by using the filter bank; $\boldsymbol{v}$ denotes the sparse coefficient. In problem (8), the term $\|\boldsymbol{v} - \boldsymbol{W}\boldsymbol{x}\|_2{}^2$ can make sure that the sparse coefficient $\boldsymbol{v}$ is in close proximity to the sparse coefficient of the image $\boldsymbol{x}$ under the adaptive tight frame $\boldsymbol{W}$; the term $\|\boldsymbol{v}\|_0$ can ensure the sparsity of the coefficient $\boldsymbol{v}$; the constraint term $\boldsymbol{W}^{\mathrm{T}}\boldsymbol{W} = \mathbf{I}$ is used to guarantee that $\boldsymbol{W}$ satisfies the tight frame property.

In [20], a DDTF-based CSMRI algorithm was introduced to reconstruct MR images, and the minimization problem of the algorithm is shown as the following formulation

$$\min_{\boldsymbol{x},\boldsymbol{W}} \|\boldsymbol{W}\boldsymbol{x}\|_1 s.\ t.\ \|\boldsymbol{y} - \boldsymbol{F}_u\boldsymbol{x}\|_2^2 \le \sigma^2,\ \boldsymbol{W}^{\mathrm{T}}\boldsymbol{W} = \mathbf{I}, \tag{9}$$

where σ stands for the noise standard deviation. Problem (9) aims at effectively enhancing the sparsity of the MR image in tight frame domain by ATF learning, and then recovers the MR image. In addition, problem (9) was solved by using the two-level Bregman iterative method [20], and the excellent performance of MR image reconstruction was attained.

3. The proposed TFGS and CD-MRI

3.1. The proposed TFGS formulation

In order to better sparsely represent the structures of images, we fuse the advantages of the ATF learning technique and group sparsity, then present tight frame-based group sparsity (TFGS) regularization which represents the adaptive group sparsity of images by using ATF learning technique. Mathematically, we formulate the optimization problem of TFGS as follows

$$\min_{\boldsymbol{W},\boldsymbol{\alpha}} \frac{1}{2} \|\boldsymbol{x} - \boldsymbol{W}^{\mathrm{T}}\boldsymbol{\alpha}\|_2^2 + \lambda \sum_j \Phi(\|\boldsymbol{\alpha}_j\|_2; \mathrm{C})\ s.\ t.\ \boldsymbol{W}^{\mathrm{T}}\boldsymbol{W} = \mathbf{I}, \tag{10}$$

where $\boldsymbol{W}$ is the adaptive tight frame which directly learns from images, and the superscript T indicates the transpose operation of the matrix. $\boldsymbol{\alpha}$ is the sparse coefficient, and $\boldsymbol{\alpha}_j$ designates the sparse coefficient for the jth sparse group. C is the positive parameter. $\Phi(\bullet;\mathrm{C})$ represents parameterized penalty function [44], and it is defined as the arctangent penalty as follows

$$\Phi(\cdot;\mathrm{C}) = \frac{2}{\sqrt{3}\mathrm{C}}\left(\tan^{-1}\left(\frac{1 + 2\mathrm{C}|\cdot|}{\sqrt{3}}\right) - \frac{\pi}{6}\right). \tag{11}$$

In problem (10), the second term is a penalty function in the form of the arctangent. And, the second term not only can be used for group sparse representations of images, but also can be used to learn $\boldsymbol{W}$. Moreover, the first term in problem (10) denotes the data fidelity, and is used to well adjust the error. Problem (10) can make full use of the intrinsic priors of images, and capture more group structure information of images. Hence, TFGS has good group sparse representation performance for MR images.

3.2. The proposed CD-MRI algorithm

In this section, the proposed TFGS formulation is employed to the image cartoon-texture decomposition framework for reconstructing MR images. Because the image cartoon-texture decomposition model is devoted to optimal representations for cartoon and texture components of images, TV regularization can provide gradient-based global sparse representation for the cartoon part of the image, and the proposed TFGS regularization can achieve better adaptive group sparse representation for the texture part. Thereupon, in order to exploit more effective sparse priors to further improve the quality of the MR image reconstruction, we propose a new MR image reconstruction algorithm denominated CD-MRI by focusing on amalgamating TV and the proposed TFGS regularization into the image cartoon-texture decomposition model. The corresponding optimization problem of the proposed CD-MRI can be formulated as

$$\min_{\boldsymbol{x},\boldsymbol{x}_c,\boldsymbol{W},\boldsymbol{\alpha}} \frac{1}{2}\|\boldsymbol{x}-\boldsymbol{x}_c-\boldsymbol{W}^{\mathrm{T}}\boldsymbol{\alpha}\|_2^2+\lambda_1\sum_j \Phi(\|\boldsymbol{\alpha}_j\|_2;\mathrm{C}),$$
$$+\lambda_2\mathrm{TV}(\boldsymbol{x}_c)+\frac{\tau}{2}\|\boldsymbol{F}_u\boldsymbol{x}-\boldsymbol{y}\|_2^2 s.\ t.\ \boldsymbol{W}^{\mathrm{T}}\boldsymbol{W}=\mathbf{I}, \tag{12}$$

where $\boldsymbol{x}_c$ denotes the cartoon component of the MR image. $\boldsymbol{W}$ learns from the texture component of the MR image. τ is the positive parameter. In formulation (12), the second term is used for group sparse representations of the texture component; the third term is employed to gain the global gradient sparse representations of the cartoon component. Besides, the first three terms in formulation (12) denote the constraint regularization terms of CD-MRI for the group sparsity in tight frame domain and gradient sparsity in gradient domain respectively, and can be used to pledge the edge preserving and texture properties. In a word, formulation (12) indicates that the adaptive sparse representations of image cartoon-texture decomposition model by developing gradient sparsity of cartoon components and group sparsity of texture components with ATF respectively, can guarantee to obtain minimum reconstruction error, and can achieve high-quality MR image reconstruction.

In this paper, we employ the alternating iterative minimization method to attack the optimization problem of the proposed CD-MRI. Particularly, the alternating iterative minimization process for formulation (12) is distributed into three stages: solving $\boldsymbol{\alpha}$ and $\boldsymbol{W}$ stage, solving $\boldsymbol{x}_c$ stage, and reconstructing the underlying MR image $\boldsymbol{x}$ stage. In the first stage, we tackle the sparse coefficient $\boldsymbol{\alpha}$ and the adaptive tight frame $\boldsymbol{W}$ via the following formulation with fixed $\boldsymbol{x}$ and the cartoon component $\boldsymbol{x}_c$ in formulation (12)

$$\min_{\boldsymbol{W},\boldsymbol{\alpha}} \frac{1}{2}\|\boldsymbol{x}-\boldsymbol{x}_c-\boldsymbol{W}^{\mathrm{T}}\boldsymbol{\alpha}\|_2^2+\lambda_1\sum_j \Phi(\|\boldsymbol{\alpha}_j\|_2;\mathrm{C})\ s.\ t.\ \boldsymbol{W}^{\mathrm{T}}\boldsymbol{W}=\mathbf{I}. \tag{13}$$

Here, problem (13) is equivalent to the following optimization problem owing to satisfying $\boldsymbol{W}^{\mathrm{T}}\boldsymbol{W}=\mathbf{I}$ [43].

$$\min_{\boldsymbol{W},\boldsymbol{\alpha}} \frac{1}{2}\|\boldsymbol{W}(\boldsymbol{x}-\boldsymbol{x}_c)-\boldsymbol{\alpha}\|_2^2+\lambda_1\sum_j \Phi(\|\boldsymbol{\alpha}_j\|_2;\mathrm{C})\ s.\ t.\ \boldsymbol{W}^{\mathrm{T}}\boldsymbol{W}=\mathbf{I}. \tag{14}$$

We can attack problem (14) by utilizing the alternating iterative minimization method again, and the process of solving problem (14) involves two subproblems. In the first subproblem, $\boldsymbol{\alpha}$ can be gained with fixed $\boldsymbol{W}$ as

$$\min_{\boldsymbol{\alpha}} \frac{1}{2}\|\boldsymbol{W}(\boldsymbol{x}-\boldsymbol{x}_c)-\boldsymbol{\alpha}\|_2^2+\lambda_1\sum_j \Phi(\|\boldsymbol{\alpha}_j\|_2;\mathrm{C}). \tag{15}$$

Here, if the size of group sparse coefficient is $K_1\times K_2$ for the texture component, C equals $1/(K_1K_2\lambda_1)$ [44]. The Majorization-Minimization (MM) procedure can be used to solve problem (15). Hence, for the $(k+1)$th iteration, we can acquire the following equation for solving $\boldsymbol{\alpha}^{k+1}$ by using MM procedure

$$\boldsymbol{\alpha}^{k+1}=\arg\min_{\boldsymbol{\alpha}} Q(\boldsymbol{\alpha},\boldsymbol{\alpha}^k), \tag{16}$$

where the function $Q(\cdot,\cdot)$ represents a majorizer of the cost function in problem (15), and the function $Q(\boldsymbol{\alpha},\boldsymbol{\alpha}^k)$ in problem (16) can be constructed by the following equation

$$Q(\boldsymbol{\alpha},\boldsymbol{\alpha}^k)=\frac{1}{2}\|\boldsymbol{\alpha}-\boldsymbol{W}(\boldsymbol{x}-\boldsymbol{x}_c)\|_2^2+\lambda_1\sum_j \boldsymbol{q}(\|\boldsymbol{\alpha}_j\|_2,\|\boldsymbol{\alpha}_j^k\|_2). \tag{17}$$

Here, the function $\boldsymbol{q}(\|\boldsymbol{\alpha}_j\|_2,\|\boldsymbol{\alpha}_j^k\|_2)$ in Eq. (17) is defined as [44]

$$\boldsymbol{q}(\|\boldsymbol{\alpha}_j\|_2,\|\boldsymbol{\alpha}_j^k\|_2)=\frac{1}{2\|\boldsymbol{\alpha}_j^k\|_2}\Phi'(\|\boldsymbol{\alpha}_j^k\|_2)\|\boldsymbol{\alpha}_j\|_2^2+\Phi(\|\boldsymbol{\alpha}_j^k\|_2)$$
$$-\frac{\|\boldsymbol{\alpha}_j^k\|_2}{2}\Phi'(\|\boldsymbol{\alpha}_j^k\|_2). \tag{18}$$

According to MM procedure, the function value of $Q(\boldsymbol{\alpha},\boldsymbol{\alpha}^k)$ in problem (16) is monotonically decreasing at each iteration, which assures that $\boldsymbol{\alpha}$ can converge to the minimum. Hence, we can obtain $\boldsymbol{\alpha}^{k+1}$ by using the following equation (see [44] for further details)

$$\boldsymbol{\alpha}^{k+1}=\sum_j(\boldsymbol{\alpha}_j^{k+1})=\boldsymbol{W}(\boldsymbol{x}-\boldsymbol{x}_c)/\left(1+\lambda_1\sum_j\frac{\Phi'(\|\boldsymbol{\alpha}_j^k\|_2)}{\|\boldsymbol{\alpha}_j^k\|_2}\right), \tag{19}$$

where $\boldsymbol{\alpha}_j^k$ is the sparse coefficient for the jth group in the kth iteration, and it is already calculated. Then, for the second subproblem in problem (14), $\boldsymbol{W}^{k+1}$ can be updated for the $(k+1)$th iteration via the following problem with computed $\boldsymbol{\alpha}^{k+1}$

$$\boldsymbol{W}^{k+1}=\arg\min_{\boldsymbol{W}}\frac{1}{2}\|\boldsymbol{W}(\boldsymbol{x}-\boldsymbol{x}_c)-\boldsymbol{\alpha}^{k+1}\|_2^2\ s.\ t.\ \boldsymbol{W}^{\mathrm{T}}\boldsymbol{W}=\mathbf{I}. \tag{20}$$

In order to tackle problem (20), we apply the singular value decomposition method for deducing the corresponding filters (see [43] for further details).

In the second stage for solving formulation (12) of CD-MRI, we deal with the cartoon component $\boldsymbol{x}_c$ with fixed $\boldsymbol{\alpha}$, $\boldsymbol{W}$ and $\boldsymbol{x}$, and it yields

$$\min_{\boldsymbol{x}_c}\frac{1}{2}\|\boldsymbol{x}-\boldsymbol{x}_c-\boldsymbol{W}^{\mathrm{T}}\boldsymbol{\alpha}\|_2^2+\lambda_2\mathrm{TV}(\boldsymbol{x}_c). \tag{21}$$

Problem (21) can be solved by using Chambolle's method [45].

In the third stage for solving CD-MRI, we get the desired image $\boldsymbol{x}$ by the minimization problem described as follows according to formulation (12), with fixed $\boldsymbol{\alpha}$, $\boldsymbol{W}$ and $\boldsymbol{x}_c$,

$$\min_{\boldsymbol{x}}\frac{1}{2}\|\boldsymbol{x}-\boldsymbol{x}_c-\boldsymbol{W}^{\mathrm{T}}\boldsymbol{\alpha}\|_2^2+\frac{\tau}{2}\|\boldsymbol{F}_u\boldsymbol{x}-\boldsymbol{y}\|_2^2. \tag{22}$$

Problem (22) is the least squares problem, and we receive its analytic solution written as

$$\mathbf{x}=\boldsymbol{F}^{-1}\left(\frac{\boldsymbol{F}[\boldsymbol{x}_c+\boldsymbol{W}^{\mathrm{T}}\boldsymbol{\alpha}+\tau\boldsymbol{F}_u^{\mathrm{H}}\boldsymbol{y}]}{\boldsymbol{F}\boldsymbol{F}^{\mathrm{H}}+\tau\boldsymbol{F}\boldsymbol{F}_u^{\mathrm{H}}\boldsymbol{F}_u\boldsymbol{F}^{\mathrm{H}}}\right), \tag{23}$$

where $\boldsymbol{F}$ is a normalized Fourier encoding matrix; the superscript H represents the Hermitian transpose operation; $\boldsymbol{F}\boldsymbol{F}_u{}^{\mathrm{H}}\boldsymbol{F}_u\boldsymbol{F}^{\mathrm{H}}$ is the diagonal matrix that consists of ones and zeros, and the ones of $\boldsymbol{F}\boldsymbol{F}_u{}^{\mathrm{H}}\boldsymbol{F}_u\boldsymbol{F}^{\mathrm{H}}$ tally with the sampled locations in K-space [1].

Resumptively, the solving process of our proposed CD-MRI is described in Table 1.

4. Simulation experiments and discussion

For evaluating the performance of CD-MRI for recovering MR images with noise, this paper utilized t2axialbrain, foot-012, Pulmonaryangio, hand and BMR2 five MR standard testing images with the size of 512×512 to perform several image reconstructing simulation experiments. The five MR standard testing images were derived from some prior works on CSMRI approaches, as shown in Fig. 1. In our simulation experiments, CD-MRI was executed with 200 iterations. We opted for each MR image block size of 8×8 (except the computation cost experiment in Section 4.2) and the maximum patch overlap $r=1$.

Table 1
The solving procedure of our proposed CD-MRI.

Input: $\boldsymbol{y}$, τ, λ_1, λ_2, K_1, K_2, iteration number J.
Output: Reconstructed MR image $\boldsymbol{x}$.

(1) **Initialization:** $\boldsymbol{x}^0=\boldsymbol{F}_u{}^{\mathrm{H}}\boldsymbol{y}$, $\boldsymbol{W}^0$, $\boldsymbol{x}_c{}^0=\boldsymbol{x}^0$.
(2) **While** stop criteria are not met, **do**
(3) **For** $k=0$ to $J-1$, **do**
(4) Update $\boldsymbol{\alpha}^{k+1}$ according to (19).
(5) Update $\boldsymbol{W}^{k+1}$ according to (20).
(6) **End for**
(7) $\mathbf{W}\leftarrow\boldsymbol{W}^{k+1}$.
(8) Solve $\boldsymbol{x}_c$ according to (21).
(9) Update $\boldsymbol{x}$ according to (23).
(10) **End while**

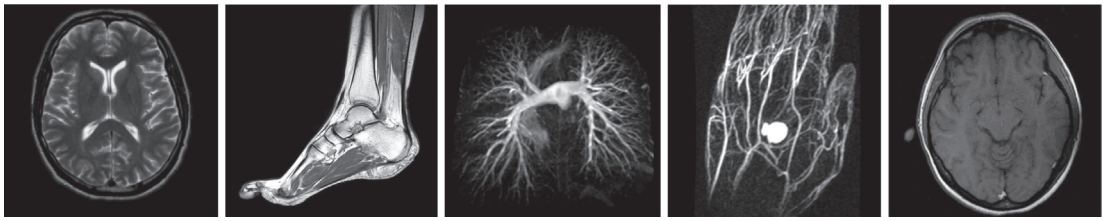

Fig. 1. MR testing images. (a) t2axialbrain, (b) foot-012, (c) Pulmonaryangio, (d) hand, (e) BMR2.

We chose with $\boldsymbol{W}$ block size of 64 × 64. We applied 12,800 patches for learning $\boldsymbol{W}$, which was performed with 30 iterations. We selected the zero-mean white Gaussian noise as the observation noise of the MR image, and its standard deviation σ was set as 5 or 10. We applied the initial MR image as the initialized cartoon component $\boldsymbol{x}_c$. We took the peak signal-to-noise ratio (PSNR in dB) [46] and the high-frequency error norm (HFEN) [1] as two metrics to check the quality of the MR image reconstruction. The PSNR value of the reconstructed image $\boldsymbol{x}$ with the size of 512 × 512 is defined as

$$\mathrm{PSNR} = 20\log_{10}(512/\|\boldsymbol{x} - \boldsymbol{x}_{org}\|_2), \tag{24}$$

where $\boldsymbol{x}_{org}$ denotes the original MR image.

Lots of simulation experiments affirmed that the high quality image reconstruction can be achieved when the parameters were set as $\lambda_1 = 0.01$, $\lambda_2 = 0.003$, $K_1 = 5$, $K_2 = 5$ for CD-MRI. In order to achieve excellent MR image reconstruction performance, the parameter τ in CD-MRI was tuned separately along with different sampling rates. We employed DLMRI [1], pFISTA [22] and the nonlocal low-rank regularization CSMRI (NLR-CS) [47] algorithms to compare with our proposed CD-MRI. DLMRI, pFISTA and NLR-CS are the better MR image reconstruction algorithms of CS kingdom in recent years. For making a fair comparison, we carefully adjusted parameters of competing algorithms in order to achieve the best possible image reconstruction performance with different CS sampling rates and sampling schemes.

4.1. Simulation experiments of MR image reconstruction performance with noise

To check the image reconstruction quality and anti-noise performance of CD-MRI under diverse sampling schemes and different noise levels, we performed various simulation experiments to reconstruct MR images with white Gaussian noise by employing 2D variable density random sampling (the sampling rate R is equal to 5% or 10%) and pseudo radial sampling (the number of sampling line l equals 60 or 110), respectively. The PSNR values of CD-MRI were compared with each competing algorithm respectively, as shown in Table 2. From Table 2, it can be seen that PSNR values of the reconstructed each image by CD-MRI are larger than each of competing algorithms in different sampling rates, sampling schemes and standard deviations of noise. Therefore, our CD-MRI can effectively improve the reconstruction precision of MR images, and can achieve superior anti-noise performance. In Table 2, we take foot-012 image as an example. It can be observed that PSNR values of the reconstructed image via CD-MRI increase by 2.91 dB, 1.89 dB and 1.04 dB respectively, compared to DLMRI, pFISTA and NLR-CS under $R = 10\%$, $\sigma = 10$ and the parameter $\tau = 0.45$ by utilizing 2D variable density random sampling. And, PSNR values of the reconstructed image of CD-MRI increase by 2.96 dB, 1.72 dB and 1.01 dB respectively, compared with DLMRI, pFISTA and NLR-CS under $l = 110$, $\sigma = 10$ and the parameter $\tau = 1$ by using pseudo radial sampling. Hence, CD-MRI can achieve excellent quality of the MR image reconstruction, and remove noise effectively.

In order to verify the superiority of CD-MRI, Fig. 2 shows that PSNR values of the reconstructed foot-012 image vary with iterations by employing different algorithms in 2D variable density random sampling mode ($R = 10\%$, $\sigma = 5$). With the same conditions as Fig. 2, Fig. 3 exhibits that HFEN values of the four algorithms vary with iterations. From Figs. 2 and 3, it can be observed that PSNR value of CD-MRI is larger than that of each competing algorithm at the last iteration, and finally CD-MRI obtains the smaller HFEN value which reveals the finer edge structure feature of reconstructed foot-012 image compared with DLMRI, pFISTA and NLR-CS. Fig. 4 depicts that PSNR values of the t2axialbrain image recovered by the four algorithms change with the different sampling rates under 2D variable density random sampling mode whose sampling rates are selected with 5%, 10%, 13%, 17%, 25%, respectively ($\sigma = 5$). Fig. 4 displays that PSNR values of CD-MRI (the parameter τ was tuned carefully) are much larger than those of the three competing algorithms. Furthermore, as shown in Fig. 4, we can see that CD-MRI can remarkably improve the quality of the

Table 2
Comparisons of the MR image reconstruction PSNR values (dB) by different algorithms.

Images	Algorithms	2D variable density random sampling				Pseudo radial sampling			
		$\sigma = 5$		$\sigma = 10$		$\sigma = 5$		$\sigma = 10$	
		$R = 5\%$	$R = 10\%$	$R = 5\%$	$R = 10\%$	$l = 60$	$l = 110$	$l = 60$	$l = 110$
t2axial-brain	DLMRI	34.62	37.51	33.88	35.52	33.08	36.23	32.22	33.89
	pFISTA	35.06	38.28	33.98	36.22	32.10	37.19	31.48	34.91
	NLR-CS	33.44	39.16	32.91	36.70	35.83	37.59	34.53	37.42
	CD-MRI	38.31	40.82	36.02	37.89	36.61	39.01	35.18	38.35
Foot-012	DLMRI	30.88	33.39	30.57	32.46	28.92	32.28	28.50	30.96
	pFISTA	31.54	34.75	30.96	33.48	28.89	33.55	28.44	32.20
	NLR-CS	29.56	35.73	28.75	34.33	32.15	34.27	31.37	32.91
	CD-MRI	33.99	37.85	32.66	35.37	32.89	35.53	31.91	33.92
Pulmonaryangio	DLMRI	36.51	39.45	35.71	36.98	33.10	37.40	32.37	34.76
	pFISTA	36.41	39.92	35.30	37.51	32.17	37.89	31.77	35.98
	NLR-CS	34.90	40.13	33.52	37.52	33.90	38.03	33.27	37.43
	CD-MRI	39.64	41.80	37.18	38.84	34.47	39.05	33.76	37.97

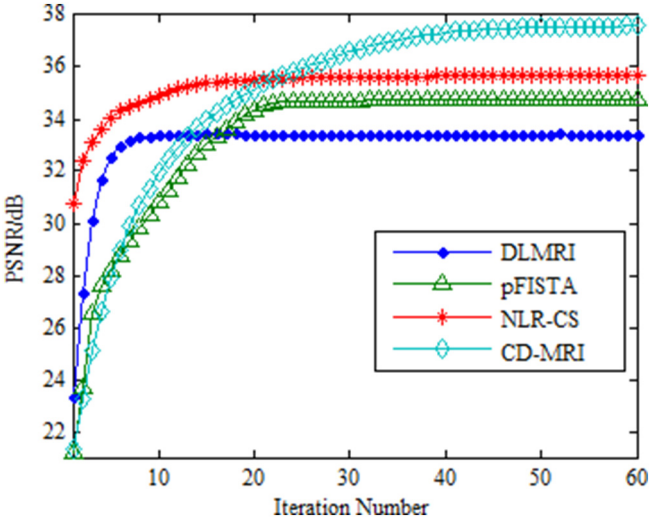

Fig. 2. PSNR curves of foot-012 image change along with iterations.

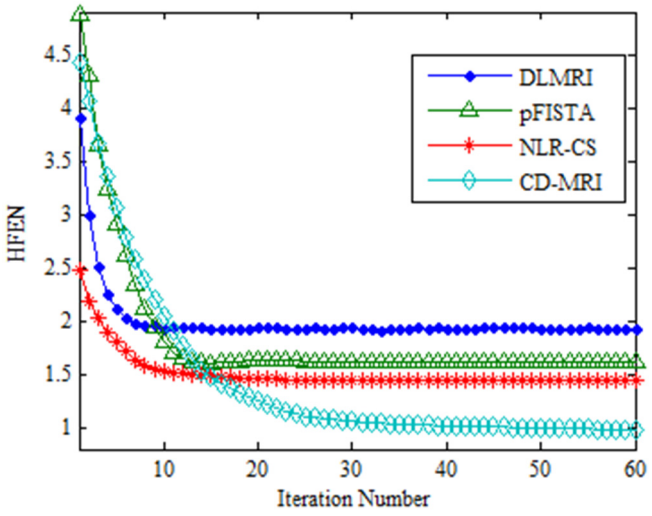

Fig. 3. HFEN curves of foot-012 image change along with iterations.

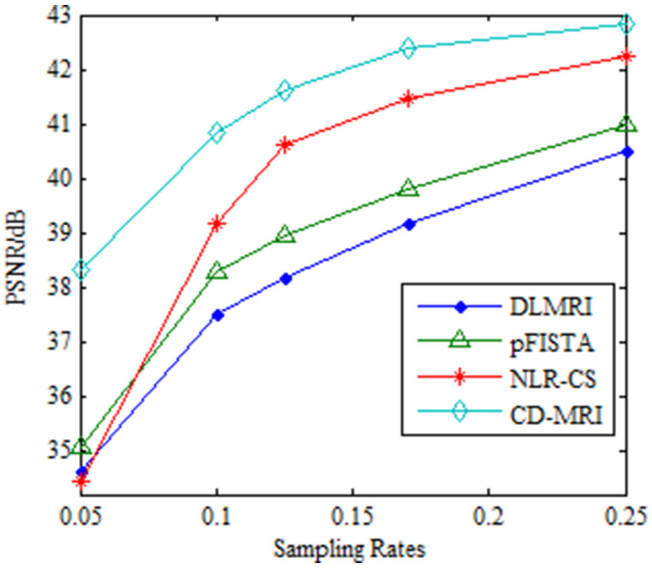

Fig. 4. PSNR curves of t2axialbrain image change with respect to different sampling rates.

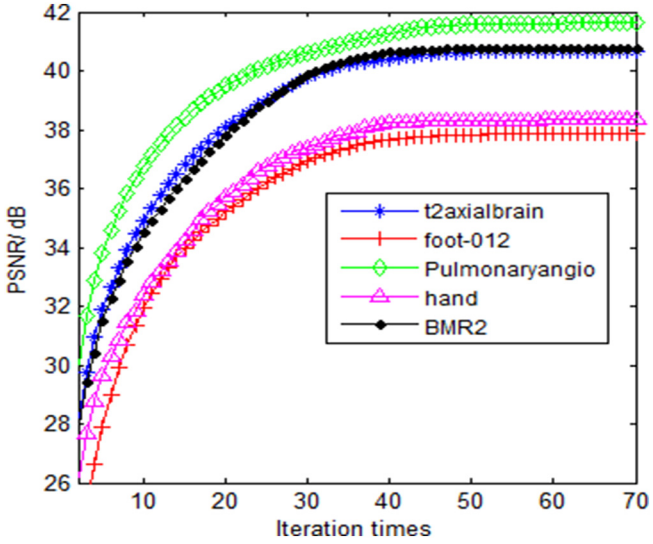

Fig. 5. PSNR curves of five MR testing images change with the number of the iteration.

reconstructed image when the sampling rate of the t2axialbrain image decreases. Hence, CD-MRI can achieve nicely image reconstruction performance at various sampling rates after a certain iteration number.

Theoretically, the proposed CD-MRI can receive more accurate global optimal solution and possess good convergence property under a certain iteration times. To prove the convergence behavior of CD-MRI, we draw PSNR curves of five reconstructed images along with the iteration times. Empirically, if the PSNR values of a curve ultimately attain the stable state with the iteration increasing, CD-MRI is convergent. Fig. 5 reveals five PSNR curves versus iterations for the five MR testing images in Fig. 1 under 2D variable density random sampling pattern with the sampling rate $R = 10\%$ and the noise standard deviation $\sigma = 5$. The parameter τ is set as 1. In Fig. 5, we can clearly discern that with the iteration times increasing, PSNR curves of the five MR testing images by using CD-MRI increase monotonically, and finally get stable. Therefore, we can deduce that CD-MRI has good convergence performance for reconstructing different MR images.

4.2. Comparison of computation cost

For confirming the consuming time of CD-MRI, we conducted simulation experiments on the four algorithms using MATLAB R2014a, and tested on a Lenovo computer furnished with 64 bit Windows 7 operating system, 16 GB RAM and Intel 3.40 GHz CPU. Table 3 lists the arithmetic mean CPU time of four algorithms in each iteration condition, which is expended on reconstructing the Pulmonaryangio image by using pseudo radial sampling. We opted for the Pulmonaryangio image block size of 6×6. From Table 3, we can clearly discern that NLR-CS costs the longest time; DLMRI consumes the second longest time; pFISTA takes the shortest time which is about $108\times$ and $70\times$ lower than that of NLR-CS and DLMRI respectively under the number of sampling line $l = 60$; the time of our proposed CD-MRI elapses between pFISTA and DLMRI. The expended mean CPU time of CD-MRI is about $11.5\times$ and $7.4\times$ lower than for NLR-CS and DLMRI respectively, and about $9.4\times$ higher than for pFISTA under $l = 60$ condition. As shown in

Table 3
Mean CPU cost time (s) of four algorithms in each iteration condition.

Sampling line number	DLMRI	pFISTA	NLR-CS	CD-MRI
$l = 60$	12.54	0.18	19.41	1.69
$l = 110$	15.16	0.19	19.93	1.87

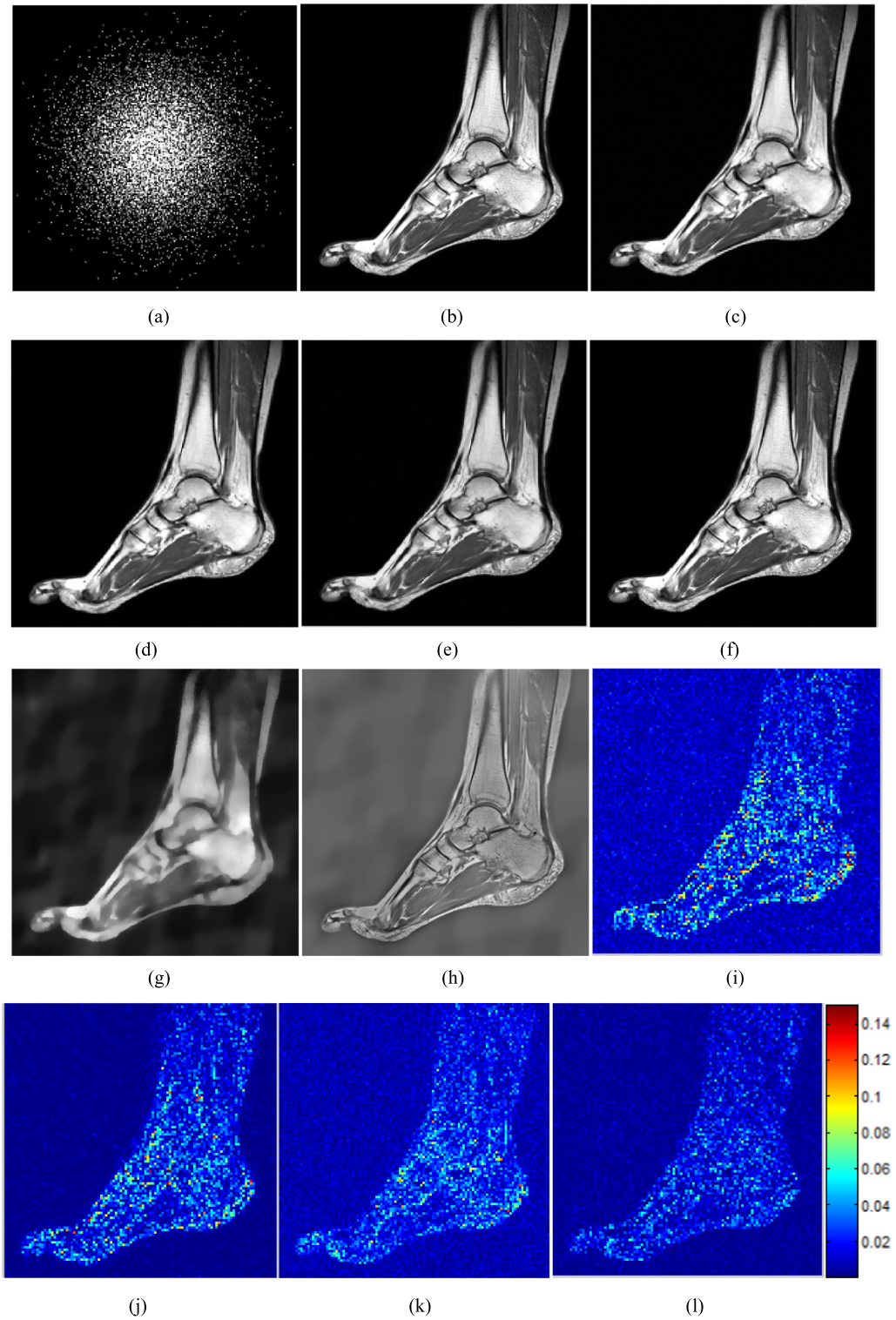

Fig. 6. Reconstructed results and error magnitudes of the foot-012 image using 2D variable density random sampling mode. (a) Sampling in K-space. (b) Original image. (c)–(f) are image reconstruction results of DLMRI, pFISTA, NLR-CS and CD-MRI, respectively. (g) Reconstructed cartoon image. (h) Reconstructed texture image. (i)–(l) are image reconstruction error magnitudes of DLMRI, pFISTA, NLR-CS and CD-MRI, respectively.

Tables 2 and 3, although CD-MRI takes longer time than that of pFISTA, the quality of the MR image reconstruction using CD-MRI is higher than for pFISTA; although the image reconstruction quality of CD-MRI is sometimes a litter bit better than that of NLR-CS under pseudo radial sampling, the consuming time of CD-MRI is always much shorter than for NLR-CS. Therefore, CD-MRI can achieve the best reconstruction accuracy of the Pulmonaryangio image without sacrificing too long time.

4.3. Simulation experiment of perceptual visual inspection

To further illustrate the validity of the proposed CD-MRI, the quality of reconstructed foot-012 image was investigated from the perceptual visual inspection. Fig. 6 exhibits experimental results of the

reconstructed foot-012 image achieved by using four algorithms with noise (standard deviation $\sigma = 5$) under 2D variable density random sampling mode (sampling rate $R = 10\%$). For the visual comparison, we can see from Fig. 6 that all of DLMRI, pFISTA, NLR-CS and CD-MRI algorithms can almost reconstruct the desired foot-012 image from the undersampled data. However, simulation experiment results using DLMRI and pFISTA lose some of the details. Meanwhile, DLMRI and pFISTA cause edge contour structures of the reconstructed image to become a bit ambiguous. The reconstruction result of NLR-CS is better than that of DLMRI or pFISTA, but it still loses a few of the details, and the edge contour structures of the reconstructed image become farther clarity. The quality of the foot-012 image reconstructed by CD-MRI (the parameter $\tau = 1$) is the best of the four algorithms. As can be seen from Figs. 6(f) and (l) that CD-MRI can obviously improve the accuracy of the image reconstruction, preserve more details, achieve sharper edge contour structures, and preferably delineate cartoon and texture features of the reconstructed image. Besides, noise in the reconstructed result is not obvious. Hence, compared with three competing algorithms, CD-MRI can acquire superior performance for reconstructing MR images and removing noise. Fig. 6(g) reveals the cartoon component of the reconstructed image via exploiting the gradient sparsity of TV; Fig. 6(h) displays the texture component reconstruction result which is obtained by employing the adaptive group sparse representations of TFGS consisted of ATF and group sparsity. It can be seen from Figs. 6(g) and (h) that edge contour structures and cartoon components can be validly reconstructed, the rest of components can be better gained, and finally the foot-012 image can be effectively reconstructed by CD-MRI. Therefore, the proposed algorithm can receive reconstruction effectiveness and better robustness for achieving well performance of the reconstructed MR image.

In summary, all the above simulation experiment results illustrate that CD-MRI significantly outperforms DLMRI, pFISTA and NLR-CS at image reconstruction performance. This is because that CD-MRI exploits the gradient sparsity of TV regularization to reconstruct the cartoon component, utilizes group sparse priors with respect to TFGS regularization to capture more local texture structure features for reconstructing the texture component, and coalesces the cartoon-texture decomposition model to further promote the quality of the MR image reconstruction. Virtually, TV regularization has good abilities of the gradient sparsity and preserving preferable edge structure features, simultaneously the group sparse regularization by TFGS fused ATF learning and group sparse representation can adapt to the texture component, and ATF learning approach can boost up the adaptability of CD-MRI. In virtue of different sparse representation methods, the sparse representation effectiveness is different for different components of the MR image. Therefore, in this paper, the proposed CD-MRI based on TV regularization, TFGS and image cartoon-texture decomposition model can achieve remarkably superior reconstruction precision of MR images, faster reconstruction speed than for DLMRI and NLR-CS, much better robustness to noise, more edge contour structure features and detail information of the MR image.

5. Conclusion

In this paper, we presented the TFGS regularization for better group sparse representing MR images, then TFGS regularization was used to the image cartoon-texture framework to obtain a novel CD-MRI algorithm. CD-MRI can utilize the gradient sparsity of TV regularization for the cartoon component, and employ the adaptive group sparse representation of TFGS regularization for the texture component. That is, the advantages of CD-MRI are that CD-MRI applies both the global gradient sparse priors of the cartoon component as well as the group sparse priors of the texture component to reconstruct MR images. The proposed CD-MRI can be effectively solved by the alternating iterative minimization method imbedded MM algorithm. Compared with DLMRI, pFISTA and NLR-CS, various simulation experiment results have manifested that our proposed CD-MRI can achieve better performance for reconstructing MR images in detail clarity, edge contour structure preservation and noise suppression via the quantitative and qualitative visual assessment. Hence, CD-MRI has the ability for implementing highly accurate image reconstruction over the competing algorithms by employing different sampling schemes and noise levels. The reason is that CD-MRI is able to perform superior sparse representations respectively for the cartoon and texture components of MR images in essence. Moreover, it can be conducive to the clinical application of MR images by using CD-MRI. How to further develop more effective sparse priors for reconstructing MR images, and how to further achieve accurately and fast MR image reconstruction in term of much lower sampling rate are our research aspects in the future.

Acknowledgments

This work was supported by China NSFC 61471313, Science and Technology Major Special Project of Anhui Province 18030901022 and Scientific Research and Development Program of Qinhuangdao 201805A003. We sincerely would like to acknowledge the financial supports.

References

[1] Ravishankar S, Bresler Y. MR image reconstruction from highly undersampled space data by dictionary learning. IEEE Trans Med Imaging 2011;30(5):1028–41.
[2] Fan X, Lian Q, Shi B. Compressed sensing MRI with phase noise disturbance based on adaptive tight frame and total variation. IEEE Access 2017;5:19311–21.
[3] Woods JC, Conradi MS. ^{3}He diffusion MRI in human lungs. J Magn Reson 2018;292:90–8.
[4] Donoho DL. Compressed sensing. IEEE Transactions on Information Theory 2006;52(4):1289–306.
[5] Candes E, Roberg J, Tao T. Robust uncertainty principles: exact signal recognition from highly incomplete frequency information. IEEE Transactions on Information Theory 2006;52(2):489–509.
[6] Zhang Y, Yang J, Yang J, Liu A, Sun P. A novel compressed sensing method for magnetic resonance imaging: exponential wavelet iterative shrinkage-thresholding algorithm with random shift. International Journal of Biomedical Imaging 2016;3:1–10.
[7] Ravishankar S, Bresler Y. Efficient blind compressed sensing using sparsifying transforms with convergence guarantees and application to magnetic resonance imaging. SIAM Journal on Imaging Sciences 2015;8(4):2519–57.
[8] Liu Y, Cai JF, Zhan Z, Guo D, Ye J, Chen Z, et al. Balanced sparse model for tight frames in compressed sensing magnetic resonance imaging. PLoS One 2015;10(4):1–19.
[9] Huang J, Guo L, Feng Q, Chen W, Feng Y. Sparsity-promoting orthogonal dictionary updating for image reconstruction from highly undersampled magnetic resonance data. Phys Med Biol 2015;60(14):5359–80.
[10] Lustig M, Donoho D, Pauly J. Sparse MRI: the application of compressed sensing for rapid MR imaging. Magn Resonance Med 2007;58(6):1182–95.
[11] Kim Y, Altbach M, Trouard T, Bilgin A. Compressed sensing using dual-tree complex wavelet transform. Proceedings of the International Society for Magnetic Resonance in Medicine, USA 2009;17:2814.
[12] Qu X, Zhang W, Guo D, Cai C, Cai S, Chen Z. Iterative thresholding compressed sensing MRI based on contourlet transform. Inverse Problems in Science and Engineering 2010;18(6):737–58.
[13] Qu X, Cao X, Guo D, Hu C, Chen Z. Combined sparsifying transforms for compressed sensing MRI. Electronics Letters 2010;46(2):121–3.
[14] Huang J, Zhang S, Metaxas D. Efficient MR image reconstruction for compressed MR imaging. Med Image Anal 2011;15(5):670–9.
[15] Chen C, Huang J. Compressive sensing MRI with wavelet tree sparsity. Nevada, USA: NIPS; 2012. p. 1124–32.
[16] Huang J, Liu W, Wang L, Zhu Y. Combining total variation with nonlocal self-similarity constraint for compressed sensing MRI. IEEE 11th international symposium on biomedical imaging, Beijing, China. 2014. p. 1063–6.
[17] Ravishankar S, Bresler Y. Sparsifing transform learning for compressed sensing MRI. IEEE international symposium on biomedical imaging: from nano to macro, San Francisco, USA. 2013. p. 17–20.
[18] Liu Q, Wang S, Ying L, Peng X, Zhu Y, Liang D. Adaptive dictionary learning in sparse gradient domain for image recovery. IEEE Transaction on Image Processing 2013;22(12):4652–63.
[19] Ding X, Paisley J, Huang Y, Chen X, Huang F, Zhang XP. Compressed sensing MRI with Bayesian dictionary learning. IEEE international conference on image processing. 2014. p. 2319–23. Melbourne, Australia.
[20] Liu J, Wang S, Peng X, Liang D. Undersampled MR image reconstruction with data-driven tight frame. Comput Math Methods Med 2015;1:424087.
[21] Wang S, Liu J, Xi P, Dong P, Liu Q, Liang D. Two-layer tight frame sparsifying model for compressed sensing magnetic resonance imaging. Biomed Res Int 2016:1–7.

[22] Liu Y, Zhan Z, Cai JF, Guo D, Chen Z, Qu X. Projected iterative soft-thresholding algorithm for tight frames in compressed sensing magnetic resonance imaging. IEEE Trans Med Imaging 2016;35(9):2130–40.
[23] Xiong J, Lu H, Zhang M, Liu Q. Convolutional sparse coding in gradient domain for MRI reconstruction. Acta Automatica Sinica 2017;43(10):1841–9.
[24] Xiong J, Liu Q, Wang Y, Xu X. A two-stage convolutional sparse prior model for image restoration. Journal of Visual Communication & Image Representation 2017;48:268–80.
[25] Huang J, Huang X, Metaxas D. Learning with dynamic group sparsity. IEEE international conference on computer vision, Japan. 2009. p. 64–71.
[26] Jin X, Jiang MF, Feng J. Group sparsity regularization based compressed sensing MR image reconstruction. Adv Mat Res 2014;989–994:3946–51.
[27] Jiang M, Liu Y, Xu W, Hu J, Wang Y, Gong Y, et al. Efficient compressed sensing reconstruction using group sparse total variation regularization. Journal of Medical Imaging & Health Informatics 2015;5(5):907–17.
[28] Liu S, Cao J, Liu H, Zhou X, Zhang K, Li Z. MRI reconstruction via enhanced group sparsity and nonconvex regularization. Neurocomputing 2017;272(1):108–21.
[29] Liu RW, Shi L, Yu SCH, Wang D. Hybrid regularization for compressed sensing MRI: exploiting shearlet transform and group-sparsity total variation. The 20th IEEE international conference on information fusion, Xi an, China. 2017. p. 17102499.
[30] Yu H, Jiang M, Chen H, Feng J, Wang Y, Lu Y. Super-pixel algorithm and group sparsity regularization method for compressed sensing MR image reconstruction. Optik 2017;140:392–404.
[31] Meyer Y. Osillating patterns in image processing and non-linear evolution equation. Boston, USA: American Mathematical Society; 2002.
[32] Elad M, Starck JL, Donoho D, Querre P. Simultaneous cartoon and texture image inpainting using morphological component analysis (MCA). Applied and Computational Harmonic Analysis 2005;19(3):340–58.
[33] Shoham N, Elad M. Algorithms for signal separation exploiting sparse representations with application to texture image separation. The IEEE 25th convention of electrical and electronics engineers in Israel, Eilat, Israel. 2008. p. 3–5.
[34] Tu S, Zhang S, Chen Y, Freedman MT, Wang B, Xuan J, et al. Automatic tracing and segmentation of rat mammary fat pads in MRI image sequences based on cartoon-texture model. Transactions of Tianjin University 2009;15(3):229–35.
[35] Peyre G, Fadili J, Starck JL. Learning the morphological diversity. SIAM J Imaging Sci 2010;3(3):646–69.
[36] Li Y, Feng X. Image decomposition via learning the morphological diversity. Pattern Recognition Letters 2012;33(2):111–20.
[37] Zhang H, Patel VM. Convolutional sparse and low-rank coding-based image decomposition. IEEE Trans Image Process 2018;27(5):2121–34.
[38] Starck JL, Elad M, Donoho DL. Image decomposition via the combination of sparse representations and a variational approach. IEEE Trans Image Process 2005;14(10):1570–82.
[39] Selesnick IW, Chen PY. Total variation denoising with overlapping group sparsity. IEEE international conference on acoustics, speech and signal processing, Vancouver, BC, Canada. 2013. p. 5696–700.
[40] Chen PY, Selesnick IW. Translation-invariant shrinkage/thresholding of group sparse signals. Signal Processing 2014;94(1):476–89.
[41] Liu J, Huang TZ, Selesnick IW, Lv XG, Chen PY. Image restoration using total variation with overlapping group sparsity. Inform Sci 2015;295:232–46.
[42] Wan L, Han G, Shu L, Feng N. The critical patients localization algorithm using sparse representation for mixed signals in emergency healthcare system. IEEE Systems Journal 2018;12(1):52–63.
[43] Cai JF, Ji H, Shen Z, Ye GB. Data-driven tight frame construction and image denoising. Applied and Computational Harmonic Analysis 2014;37:89–105.
[44] Chen PY, Selesnick IW. Group-sparse signal denoising: non-convex regularization, convex optimization. IEEE Transactions on Signal Processing 2013;62(13):3464–78.
[45] Chambolle A. An algorithm for total variation minimization and applications. Journal of Mathematical Imaging and Vision 2004;20:89–97.
[46] Shi B, Lian Q, Huang X, An N. Constrained phase retrieval: when alternating projection meets regularization. Journal of the Optical Society of America B 2018;35(6):1271–81.
[47] Dong W, Shi G, Li X, Ma Y, Huang F. Compressive sensing via nonlocal low-rank regularization. IEEE Trans Image Process 2014;23(8):3618–32.